A method for determining the constitutive model of the heat-affected zone using digital image correlation

Yan, Rui; Xin, Haohui; Yang, Fei; El Bamby, Hagar; Veljkovic, Milan; Mela, Kristo

DOI
10.1016/j.conbuildmat.2022.127981

Publication date
2022

Document Version
Final published version

Published in
Construction and Building Materials

Citation (APA)
Yan, R., Xin, H., Yang, F., El Bamby, H., Veljkovic, M., & Mela, K. (2022). A method for determining the constitutive model of the heat-affected zone using digital image correlation. *Construction and Building Materials*, *342*, Article 127981. https://doi.org/10.1016/j.conbuildmat.2022.127981

Construction and Building Materials 342 (2022) 127981

Contents lists available at ScienceDirect

Construction and Building Materials

journal homepage: www.elsevier.com/locate/conbuildmat

A method for determining the constitutive model of the heat-affected zone using digital image correlation

Rui Yan [a,*], Haohui Xin [b], Fei Yang [c], Hagar El Bamby [a], Milan Veljkovic [a], Kristo Mela [d]

[a] Department of Engineering Structures, Delft University of Technology, Delft 2628 CN, The Netherlands
[b] School of Human Settlements and Civil Engineering, Xi'an Jiaotong University, Xi'an, China
[c] School of Civil Engineering, Chang'an University, Xi'an, China
[d] Faculty of Built Environment, Tampere University, Tampere, Finland

ARTICLE INFO

Keywords:
Heat-affected zone
Constitutive model
Welded coupon test
Digital image correlation
High strength steels

ABSTRACT

The heat-affected zone (HAZ) is an unmelted region of a welded joint that has changed in material properties because of high temperatures during the welding process. HAZ has a lower strength than the base (parent) material (BM) and the weld metal (WM). The lower material strength is more significant if BM is made of high strength steel and the undermatching filler metal is used. Therefore, the constitutive model of HAZ is essential for predicting the mechanical behaviour of the welded joint. In this paper, a method for determining the true stress–strain relationship of HAZ is proposed. The effect of the transverse constraint on the longitudinal deformation of HAZ imposed by BM and/or WM is eliminated by a linear modification factor correlating to the true strain. Standard tensile coupon tests were used to obtain the constitutive model of HAZ using digital image correlation (DIC). The modification factor proposed for reducing the true stress is calibrated based on finite element analysis (FEA). The modified constitutive model of HAZ is validated against the experimental results obtained by DIC. The validated HAZ material property can be used in advanced numerical simulation of welded joints.

1. Introduction

A welded joint consists of the following three major regions: the base material (BM), the heat-affected zone (HAZ), and the weld metal (WM). HAZ has the lowest material strength among all three regions. Therefore, a specific constitutive model of HAZ is crucial for predicting the behaviour of welded joints based on finite element analysis (FEA).

Generally, there are four common approaches to obtain the constitutive model of HAZ, as illustrated in [1]. The first approach is based on the empirical correlation between the Vickers hardness and the material strength [2–4] to establish an approximate stress–strain relationship. While the Vickers hardness test is easy to conduct and the result for each region is not affected by the adjacent regions, the hardness result is not directly correlated to the yield strength and the ultimate strength but associated with the stress at an approximately 8% strain [5]. The second approach is to conduct tensile tests on micro-specimens [4,6–9]. The material property for each sub-region could be directly obtained from the tensile test. However, the fabrication and testing of micro-specimens are time-consuming and costly compared to the procedure based on the standard coupon specimen. The additional practical problem is to obtain the micro-specimen with the homogeneous material. The thermal–mechanical FEA [10,11] is used in the third approach. Based on the elements' highest history temperature obtained from the thermal finite element (FE) model, unique material property is assigned to each element in the mechanical FE model. Although this approach reasonably considers the material inhomogeneity, the constitutive model of HAZ highly depends on the welding heat input and the cooling rate [12–15] instead of the highest history temperature. Proper modelling of the phase change of the material during heating and cooling is a challenging task, further complicating the use of the thermo-mechanical FEA in creating the material model of HAZ. The last approach is to test the welded coupon specimen with a butt weld in the middle transverse to the tensile loading direction [16–25]. It is essential to use the digital image correlation (DIC) technique since the local deformation in each region of the welded coupon specimen should be measured. Based on the uniform stress assumption [16] and the local deformation measured by DIC, the stress–strain relationship for HAZ is established.

Under the framework of the fourth approach, inverse methods for

* Corresponding author.
E-mail address: r.yan@tudelft.nl (R. Yan).

https://doi.org/10.1016/j.conbuildmat.2022.127981
Received 19 December 2021; Received in revised form 5 April 2022; Accepted 26 May 2022
Available online 4 June 2022

characterising the heterogeneous material property mainly fall into two categories. The first one is purely based on the full-field deformation measured by DIC. Sutton et al. [19] and Louëdec et al. [26] used the virtual fields method to identify the heterogeneous constitutive parameters in a friction stir welded joint. Besides, Sutton et al. [19] compared the virtual fields method to the uniform stress method. The same assumptions, which were the plane stress condition and the regions arranged in series, used in the uniform stress method were adopted in the virtual fields method. A very good agreement was obtained between the results from these two methods. Milosevic et al. [27,28] proposed a method to establish the true stress–strain relationship based on the DIC measurements. An analytical expression is used to correct the stress concentration in the weld zone.

The second inverse method is the finite element model updating (FEMU) method. The material constitutive parameters are characterised by an iterative process where the measured full-field data is fitted with the aid of FEA. This method can be used to determine the mechanical [29,30] and the thermal parameters [31]. A theoretical constitutive model with assumed parameters is used in FEA as the starting point of the inverse method. The result of FEA is compared to the experimental result using a cost function, and the parameters of the constitutive model are adjusted accordingly. Alternatively, instead of the cost function in FEMU, the FEA result is evaluated by visually comparing the fitting level of FEA and experimental results in a trial-and-error process [32,33].

From a structural engineering perspective, it is essential to establish a HAZ stress–strain relationship suitable for FEA of large scale welded joints, such as welded tubular joints. Further detailed region partition, such as the fine-grain heat-affected zone (FGHAZ) and the coarse-grain heat-affected zone (CGHAZ), may not be practical in the large scale joint analysis. Since HAZ comprises different types of grain, the measured stress–strain relationship before necking is not well fitted by the existing theoretical constitutive model. Hence, the measured stress–strain relationship is used as the basis for input in the analysis instead of a new theoretical constitutive model. The measured stress–strain relationship should be modified, as illustrated below, in an attempt to simplify the modelling of the HAZ effect. Given the scale of tubular joints and the FEA result difference due to the minimum parameter increment, the trial-and-error process is used in the proposed simplified method.

Two issues should be addressed to obtain the correct stress–strain relationship of HAZ. The first issue is regarding the effect of the transverse constraint on HAZ. The welded coupon specimen has a “strong” (BM and WM) and a “weak” (HAZ) region connected in series in the loading direction. The strong material would impose a transverse constraint on the weak material, resulting in a biaxial tensile stress state (for a thin specimen) or a triaxial tensile stress state (for a thick specimen) in the weak material. The von Mises stress, σ_M, written in terms of the general stresses is presented in Equation (1).

$$\sigma_M = \sqrt{\frac{1}{2}\left[(\sigma_x-\sigma_y)^2+(\sigma_y-\sigma_z)^2+(\sigma_z-\sigma_x)^2+6\left(\tau_{xy}^2+\tau_{yz}^2+\tau_{zx}^2\right)\right]} \quad (1)$$

where σ_x, σ_y, and σ_z are normal stresses in three directions. Considering the HAZ elements close to the centre of the cross-section perpendicular to the loading direction (Y direction), the influence of shear stresses τ_{xy}, τ_{yz} and τ_{zx} are very limited and is neglected in the analysis below. For a given value of σ_M, σ_y is higher under the biaxial and triaxial stress states than under the uniaxial tensile stress state (without transverse constraint). Accordingly, the measured stress (σ_y) under biaxial and triaxial stress states is higher than the yield strength in the uniaxial stress state. For example, with $\sigma_M = 100$ MPa, $\sigma_y = 100$ MPa under the uniaxial stress state while $\sigma_y = 120$ MPa if σ_x and σ_z are 20 MPa under the triaxial tensile stress state. Lockwood et al. [18] compared the yield strength of different regions in a butt-welded thick (around 8 mm) specimen and a thin (2.5 mm, milled from the thick specimen) specimen. The thin specimen has a lower and higher yield strength in the weak (HAZ) and the strong (BM and WM) region, respectively, compared to the thick specimen. It indicates that the transverse constraint exists in the thickness direction of the thick specimen at the onset of yielding. Hochhauser et al. [15] found that the tensile strength of the thick specimen is higher than that of the thin specimen due to the transverse constraint in the thickness direction at the onset of necking. Hence, the transverse constraint in the thickness direction may exist during the entire loading process if HAZ has a lower yield and tensile strength than BM and WM. Similarly, the transverse constraint would also exist in the width direction of the milled thin specimen. Therefore, the stress–strain relationship of HAZ measured by DIC has a higher stress at the strain hardening stage than the real material property.

The second issue is about the gauge length used for measuring the deformation of HAZ as the boundary of HAZ is not visible on the specimen in DIC. Yan et al. [1] proposed a method to evaluate the transverse constraint at the boundary of two regions using DIC. Six milled coupon specimens (3 mm thickness) with a butt weld in the middle were tested in tension. The major (along the loading direction) and minor strain were extracted from the individual points along the loading direction. The slope of the minor-major strain relationship for each measuring point at the plastic stage is used to identify the boundary of HAZ. Consequently, the virtual extensometer, which measures the deformation between two points in DIC, is created within the identified boundaries for HAZ and WM.

In this paper, the constitutive model of HAZ is developed to account for the transverse constraint imposed by the material differences among the BM, WM, and HAZ. The aim is to provide an improved material model that can be used in advanced simulation of welded tubular joints involving high strength steels, in particular. The study consists of experiments and numerical simulations. Firstly, standard tensile coupon tests were conducted on BM, using six square hollow sections (SHS) made of three steel grades (S355, S500, and S700) and two thicknesses (8 mm and 10 mm). Then, the milled welded coupon specimen (3 mm thickness) extracted from the welded SHS were tested in tension. A matching, overmatching, and undermatching electrode was used in S355, S500, and S700 SHS welded joint, respectively. The engineering stress–strain relationships for HAZ and WM were obtained based on the identified regions’ boundaries [1]. Finally, FEA was carried out to calibrate a linear modification factor for reducing the true stress of the measured HAZ constitutive model. The modified stress–strain relationship is validated against the experimental results measured by DIC. The novelty of the proposed method is in a correction of the overestimated material strength by a linear modification factor. Using the modified HAZ material property, the effect of the transverse constraint on the HAZ constitutive model is eliminated. Numerical simulations demonstrate that, using the proposed method, the tensile behaviour of the welded joint can be accurately predicted by the FE model, especially for the joint with a significant strength difference between HAZ and BM/WM, such as HSS undermatching welded joints. Besides, the linear modification factor brings light onto the effect of the transverse constraint on the welded joint behaviour, which could be further used in evaluating the resistance and deformation of the welded joint made of HSS and ultra-HSS. A reduction factor for HAZ (k_{HAZ}), as introduced in prEN1993-1–12 [34], could be proposed considering different HAZ widths and HAZ/BM/WM strength combinations.

The paper is organised as follows. The experimental study and FEA are presented in Section 2 and Section 3, respectively. In Section 4, the FEA results are compared to the experimental results for each steel grade. Finally, the conclusions are drawn in Section 5.

2. Experimental program

2.1. Materials

In this research, the investigated BM is taken from cold-formed square hollow sections (SHS) including three steel grades (S355, S500, and S700) with two nominal thicknesses (8 mm and 10 mm), resulting in

Table 1
Geometric property of base materials.

Code-name	Steel grade	Profile	Nominal thickness [mm]
S355t8	S355	140 × 140 × 8	8
S355t10		160 × 160 × 10	10
S500t8	S500	140 × 140 × 8	8
S500t10		160 × 160 × 10	10
S700t8	S700	120 × 120 × 8	8
S700t10		120 × 120 × 10	10

Table 2
Mechanical property of the base material and filler metal.

Code-name	Yield strength [MPa]	Tensile strength [MPa]	A [%]
S355t8	506	536	27
S355t10	506	539	27
S500t8	580	617	25
S500t10	593	630	21
S700t8	789	861	14
S700t10	830	902	13
Carbofil 1	502	574	28
Union Nimocr	720	780	17

where A is the percentage elongation after the fracture based on the 5.65 coefficient of proportionality, according to [35].

six profiles in total. Table 1 presents the detailed information about the six profiles named by the steel grade and the nominal thickness, such as S700t8 (S700 material with 8 mm nominal thickness).

Two short tubes were butt welded, having a V groove bevel (45° with a 1 mm gap at the root) using the metal active gas (MAG) welding process. The tubes were preheated at an interpass temperature ranging from 20 °C to 200 °C to avoid hydrogen cracking. The heat input was in the range of 1 to 1.4 kJ/mm. The mechanical property of the filler metal (electrode) provided by the fabricator is presented in Table 2. In addition, the material property of BM, obtained from the standard tensile coupon test [35] as illustrated in the next section, is also shown in Table 2. The S355 tubes were welded using the filler metal Carbofil 1, while the filler metal Union Nimocr was used for welding S500 and S700 material. Based on the comparison of the material strength of the filler metal and BM, it can be concluded that a matching, overmatching, and undermatching weld type was applied to S355, S500, and S700, respectively. Table 3 summarises the nominal chemical compositions in weight percentage of the base material and the filler metal.

2.2. Experimental setup

Two types of coupon specimen were fabricated from the opposite side of the tube's longitudinal weld, as shown in Fig. 1. The standard coupon specimen only contains BM, while the welded coupon specimen includes a butt weld in the middle. Fig. 2 presents the basic dimensions of the coupon specimen, which was designed according to ISO 6892–1 [35]. The original width (b_0) of the parallel part of the coupon specimen is 10 mm and 8 mm for the tube with 8 mm and 10 mm nominal thickness, respectively. The original cross-sectional area is 80 mm^2 resulting in a 50 mm original gauge length with a 5.65 proportional coefficient, as suggested by ISO 6892–1 [35].

Prior to the tensile test, the whole welded coupon specimen was milled to a central thickness zone of 3 mm to have a perpendicular HAZ boundary through the thickness. Consequently, it is appropriate to obtain the engineering stress based on the assumption of the uniform stress in the cross-section [16]. Since the HV 0.5 hardness of HAZ doesn't show a significant variation through the thickness, as

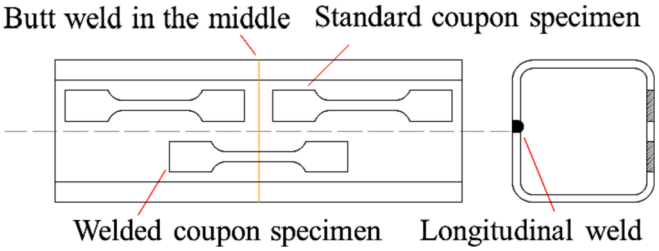

Fig. 1. Specimen cutting scheme.

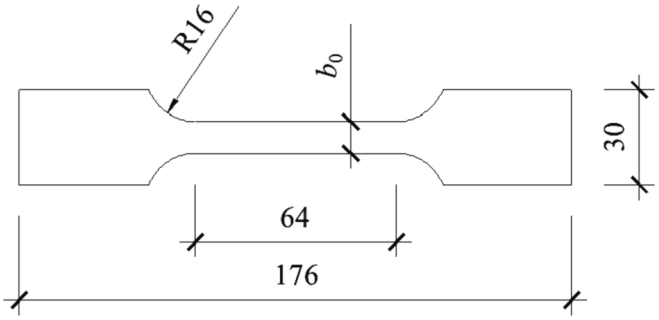

Fig. 2. Basic dimensions of the coupon specimen [mm].

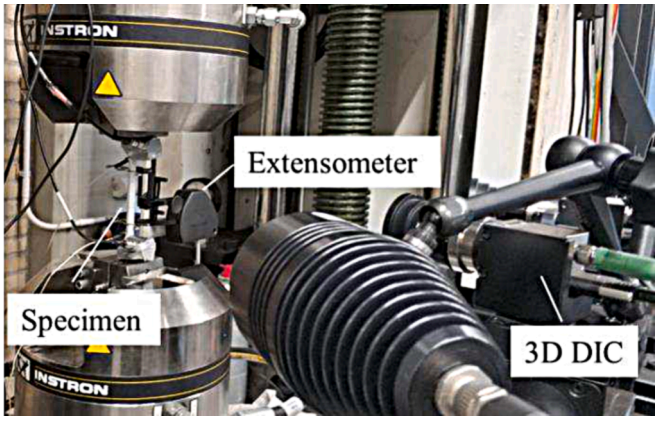

Fig. 3. Arrangement of measurements in the tensile test.

Table 3
Nominal chemical composition of the base material and the filler metal [wt%].

Code-name	C	Si	Mn	P	S	Cr	Ni	Cu	Mo	Ti	Al
S355t8	0.07	0.19	1.42	0.012	0.006	0.051	0.037	0.015	0.008	0.015	0.037
S355t10	0.08	0.19	1.43	0.012	0.004	0.040	0.036	0.013	0.002	0.018	0.037
S500t8	0.06	0.17	1.21	0.010	0.004	0.044	0.037	0.012	0.003	0.002	0.031
S500t10	0.05	0.17	1.19	0.009	0.003	0.037	0.035	0.012	0.005	0.002	0.030
S700t8	0.05	0.19	1.81	0.011	0.002	0.041	0.037	0.014	0.005	0.110	0.036
S700t10	0.06	0.18	1.81	0.011	0.003	0.045	0.034	0.012	0.005	0.113	0.041
Carbofil 1	0.078	0.85	1.45	0.008	0.004	0.03	0.01	0.01	0.01	0.02	<0.01
Union Nimocr	0.09	0.61	1.71	0.005	0.01	0.19	1.47	0.03	0.51	0.06	<0.01

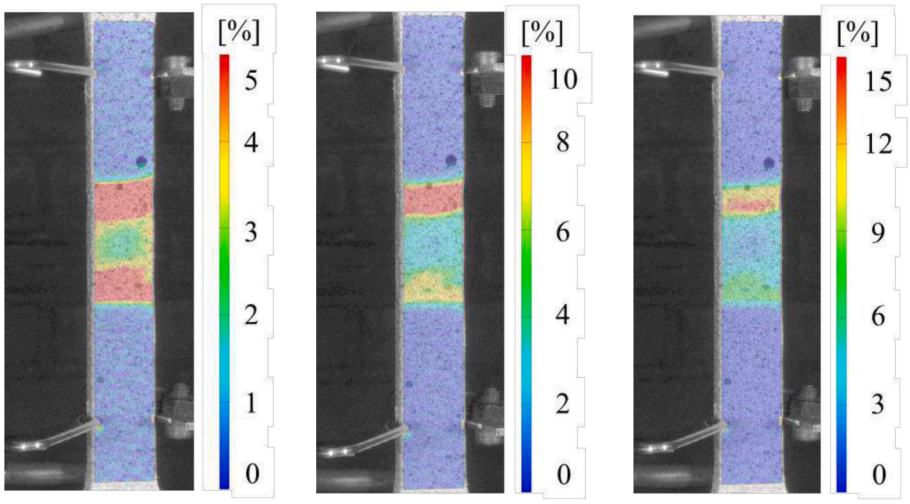

Fig. 4. Contour plots of the major strain at the ultimate load with different legend.

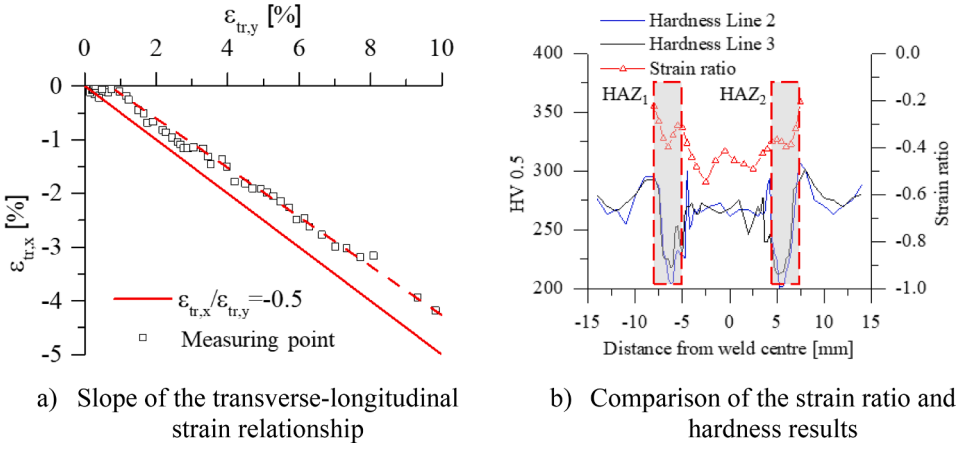

Fig. 5. Identification of the HAZ boundary.

demonstrated in the previous paper [1], the HAZ in the milled specimen could represent HAZ through the full thickness.

The standard coupon specimen and the milled welded coupon specimen were tested in an Instron testing machine with 100kN capacity. According to ISO 6892–1 [35], the loading rate was set to 0.01 mm/s with displacement control. A 50 mm extensometer and a 3D DIC (ARAMIS) were applied to measure the deformation. The arrangement of the measurements is shown in Fig. 3.

3D DIC was calibrated following the instructions from software "GOM ARAMIS professional" using the calibration panel "CP40/MV320″. The calibration was accomplished with a 0.063 pixels deviation satisfying the deviation limit of 0.1 pixels. The imaging resolution on the specimen yielded 67 μm/pixel (150 pixels for 10 mm). The DIC data was processed with a 9-pixel subset size and a 5-pixel step size [1].

3. Finite element analysis (FEA)

3.1. Uniaxial stress–strain relationship

Three major strain contour plots of the milled welded coupon specimen at the ultimate load (from S700t8 at the same loading step) are presented in Fig. 4. The only difference among the three plots is the maximum value used in the legend. Since HAZ has a lower strength than BM and WM, the high strain localises in two HAZ regions. With the maximum value in legend increasing, the width of the "red stripe" reduces, indicating that the strain cannot easily identify the boundary of HAZ. Consequently, the gauge length for measuring only the deformation of HAZ cannot be determined.

Table 4
The determined width of HAZ and WM [mm].

Code-name	S700t8	S700t10	S500t8	S500t10	S355t8	S355t10
HAZ_1	3	3.5	4	4	3	3
HAZ_2	3	2.5	4	3.5	3.5	4
WM	9.5	9	9	9	14	11.5

The method proposed by Yan et al. [1] is adopted to identify HAZ boundaries. The slope of the transverse-longitudinal strain relationship (also called strain ratio) is examined at measuring points among three regions. An example is given in Fig. 5 a) where the slope of a measuring point is compared to the ideal uniaxial state. Fig. 5 b) presents the slope and the hardness results at each measuring point of the specimen S700t8. The HAZ boundary identified by the slope of the strain matches the hardness well, indicating that the slope variation along the longitudinal direction can be used to identify the boundary. The determined widths of two HAZs, namely HAZ_1 and HAZ_2, are shown in Table 4. The

Table 5
Parameters for material property extrapolation.

Specimen	BM						WM		
	W	A	n	ε_0	a	b	A	n	ε_0
S700t8	1	949	1.91E-02	−7.46E-03	1433	845	1075	1.03E-01	−2.72E-03
S700t10	1	1000	1.85E-02	−8.11E-03	1636	889	1299	1.50E-01	1.11E-02
S500t8	0.1	672	2.00E-02	−3.85E-03	766	603	1075	1.03E-01	−2.72E-03
S500t10	0.2	851	9.00E-02	2.35E-02	554	649	940	7.35E-02	−2.77E-05
S355t8	0.6	647	3.82E-02	−3.04E-03	1746	515	982	2.12E-01	1.44E-02
S355t10	0.8	575	1.20E-02	−6.51E-03	1181	526	894	1.54E-01	−5.28E-03

HAZ deformation is measured from one of the HAZs, where the fracture appears. The gauge length is equal to the determined HAZ width.

Since the HAZ boundaries are identified, the width of WM is determined accordingly, as presented in Table 4. WM has a relatively homogeneous material. It was reported that the yield strength of WM measured from the thick and the thin specimen was very close [18], indicating that a limited transverse constraint exists in the middle of WM. Therefore, it is assumed that the effect of the transverse constraint on the longitudinal deformation does not exist at the centre 5 mm of WM. An extensometer covering the centre 5 mm of WM is used to measure the WM deformation. The load-deformation relationship of WM and HAZ is converted to an engineering stress–strain relationship based on the measured cross-section area and the gauge length. The engineering stress–strain relationship of BM is obtained from the tensile test of the standard coupon specimen with a 50 mm gauge length.

The purpose of this research is to propose a method to determine the true material property of HAZ (without the transverse constraint) for FEA. Such a model is suitable for the range before necking. The calibrated material model is useful for establishing the post-necking stress–strain relationship by extrapolating the existing theoretical models and alternative methods [36,37]. Therefore, the stress–strain relationship of HAZ, until the ultimate engineering stress, is used in FEA. A linear combination of the power law (Swift model) [38] and the linear law [39] is used to generate the BM undamaged material model, which is validated against the standard coupon test following the procedures proposed in [40]. The equations of the linear combination, the power law, and the linear law are given in Equation (2), (3), and (4), respectively.

$$\sigma_t[\varepsilon_t] = W\sigma_P[\varepsilon_t] + (1-W)\sigma_L[\varepsilon_t] \tag{2}$$

$$\sigma_P[\varepsilon_t] = A(\varepsilon_t + \varepsilon_0)^n \tag{3}$$

$$\sigma_L[\varepsilon_t] = a\varepsilon_t + b \tag{4}$$

where W is the weighting factor; A, ε_0, and n are the power law parameters; σ_P is the true stress predicted by the power law; a and b are the linear law parameters; σ_L is the true stress predicted by the linear law; σ_t and ε_t are the true stress and the true strain, respectively. Since the failure does not appear in WM, the obtained true stress-true strain relationship of WM is extended by fitting the Swift model [38]. The calibrated parameters for each specimen are shown in Table 5.

3.2. A linear stress modification factor

The welded coupon specimen consists of three materials. The "strong" (BM and WM) and "weak" (HAZ) materials connect in series along the loading direction. Since the strong material imposes a transverse constraint to the weak material during the tensile loading, the measured stress–strain relationship of the weak material cannot represent the constitutive model under the uniaxial stress state. According to the von Mises yield criterion, the transverse tensile stress (σ_x) would result in higher stress in the loading direction (σ_y) than that of the uniaxial tensile stress state at the plastic stage. Meanwhile, considering the volume preservation assumption at a plastic stage, the strain in the loading direction (ε_y) under the biaxial tensile stress state is smaller than that would be in the uniaxial stress state. Thus, the measured stress and strain, using DIC, are larger and smaller than the stress and strain measured under the uniaxial stress state, respectively.

If the measured stress–strain relationship is directly used in FEA, the predicted resistance would be higher than the experiment due to the transverse constraint in the 3D FE model. The overestimated resistance results in a higher strain in BM and WM. Consequently, the total deformation of the welded joint predicted by FEA is more significant than that of the experiment. The overestimated deformation would be even larger if a longer gauge length is used.

The extent of the transverse constraint depends on the difference in the hardening level between the strong and weak materials. With a strong BM and WM, the transverse constraint may increase with the plasticity in HAZ, such as S700 and S355 welded joints in this study. With a less strong BM and WM, the transverse constraint may vanish at the onset of necking of HAZ, such as S500 welded joints in this study. Therefore, a linear modification factor is proposed to consider different

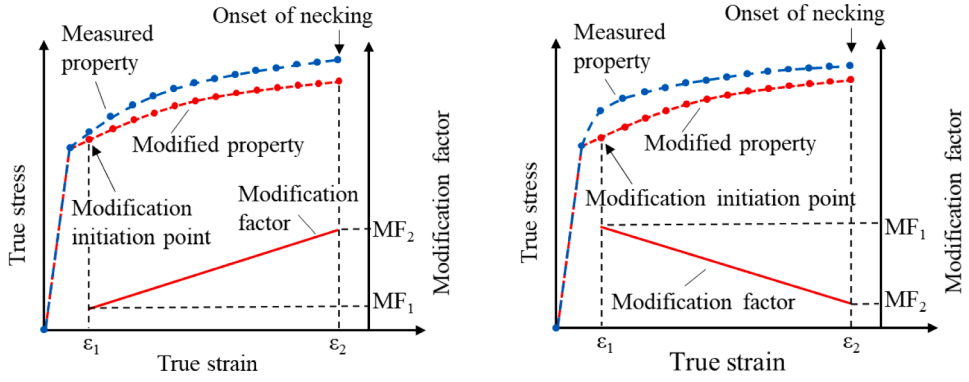

Fig. 6. Schematic diagram of the linear stress modification factor.

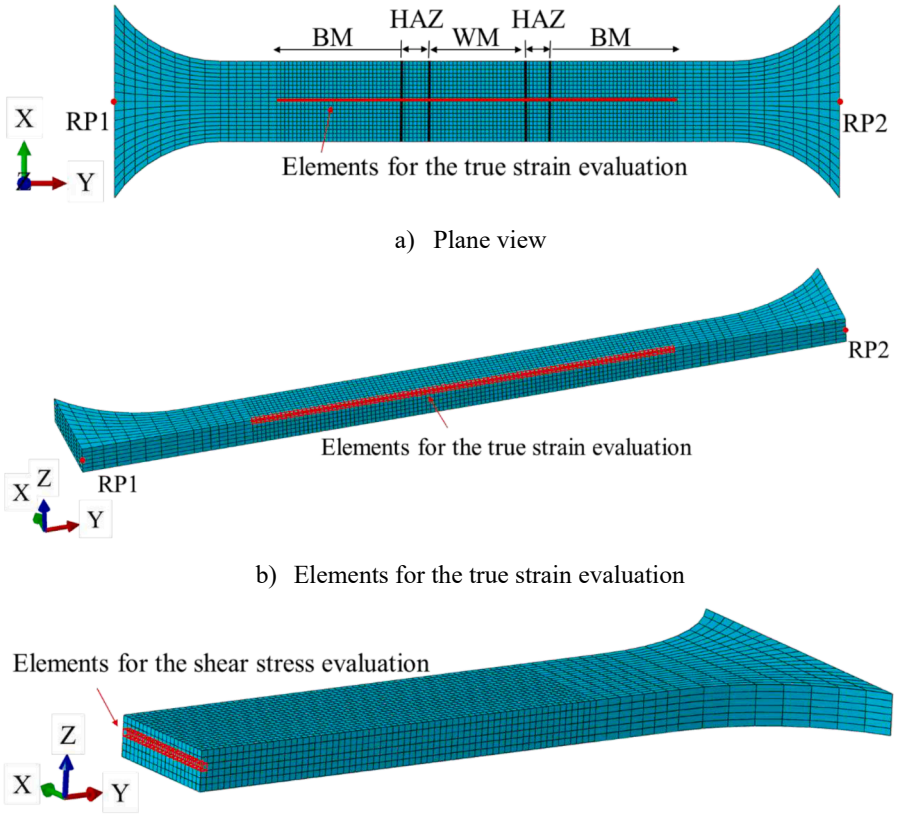

Fig. 7. FE model of the welded coupon specimen.

combinations of the materials.

At the elastic stage, Young's modulus of HAZ, BM, and WM is very close, resulting in a negligible transverse constraint at the regions' boundary. The transverse constraint appears, and the stress modification starts when HAZ yields. Two modification factors MF_1 and MF_2, which are calibrated based on FEA, are applied to the modification initiation point and the onset of necking, respectively, as shown in Fig. 6. The linear interpolation equation for the modification factor at the hardening stage is given in Equation (5). The true stress could be modified following Equation (6). It has to be emphasized that the constraint level is related to the relative hardening performance (the difference in the stress–strain stiffness) between HAZ and BM/WM. The constraint gradually increases after the proportional limit of HAZ, resulting in an increasing modification factor. The stiffness of the HAZ stress–strain relationship reduces to a relatively low and stable value at the 0.2% proof stress yield point. Therefore, as a practical approach, the yield point of HAZ is considered the modification initiation point. Besides, the ultimate stress point is taken as the onset of the necking point.

$$MF_\varepsilon = \frac{MF_2 - MF_1}{\varepsilon_2 - \varepsilon_1}(\varepsilon - \varepsilon_1) + MF_1 \tag{5}$$

$$\sigma_{\varepsilon,\text{modi}} = (1 - MF_\varepsilon)\sigma_\varepsilon \tag{6}$$

where ε_1 and ε_2 are the true strain corresponding to the modification initiation point and the onset of necking, respectively; $\sigma_{\varepsilon,\text{modi}}$ is the modified true stress. In the schematic diagram, the blue and red scatter lines represent the measured and modified true stress-true strain relationship, respectively. Note that the linear modification factor could be in an ascending or descending trend depending on the material property difference between HAZ and adjacent materials (BM and WM).

3.3. FE model

The ABAQUS:2019 software package [41] is used to conduct FEA. A 3D FE model is created for each welded coupon specimen based on the measured dimensions, as shown in Fig. 7. The model includes five parts separated by four boundaries (see black lines in Fig. 7 a)). The width of HAZ and WM is based on the experimentally determined width presented in Table 4. Note that the width could be slightly adjusted considering the accuracy of DIC results compared to hardness results presented in [1]. A 0.5 mm fine mesh in three directions is applied within the 50 mm gauge length, while a coarse mesh is used for the remaining part of the specimen. The grip parts of the specimen are not considered in the model to improve the computing efficiency. Therefore, the boundary condition is applied to the end surface. A reference point (RP) is created in the centre of each end surface. The corresponding RP controls all three translations and three rotations of the end surface through the multi-point beam constraint (MPC beam). The load is applied by a positive displacement at RP2 in the Y direction. The remaining degrees of freedom at RP1 and RP2 are constrained. The explicit solver with a 100 s period and a 0.0001 s target time increment is used to perform quasi-static analysis. The element type is the eight-node hexahedral solid element with reduced integration (C3D8R).

4. Results and discussions

A parametric study is carried out based on FEA introduced in Section 3. The load-deformation relationship (with 50 mm gauge length) and the true strain distribution (in elements in the middle of the surface marked with red colour in Fig. 7 a) and b)) are used to calibrate the modification factor MF_1 and MF_2.

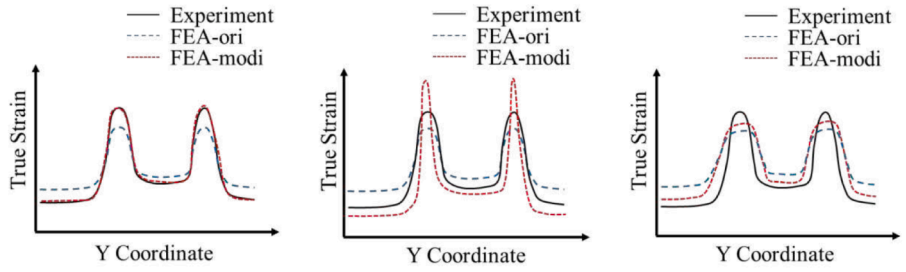

Fig. 8. Three typical longitudinal true strain distribution plots.

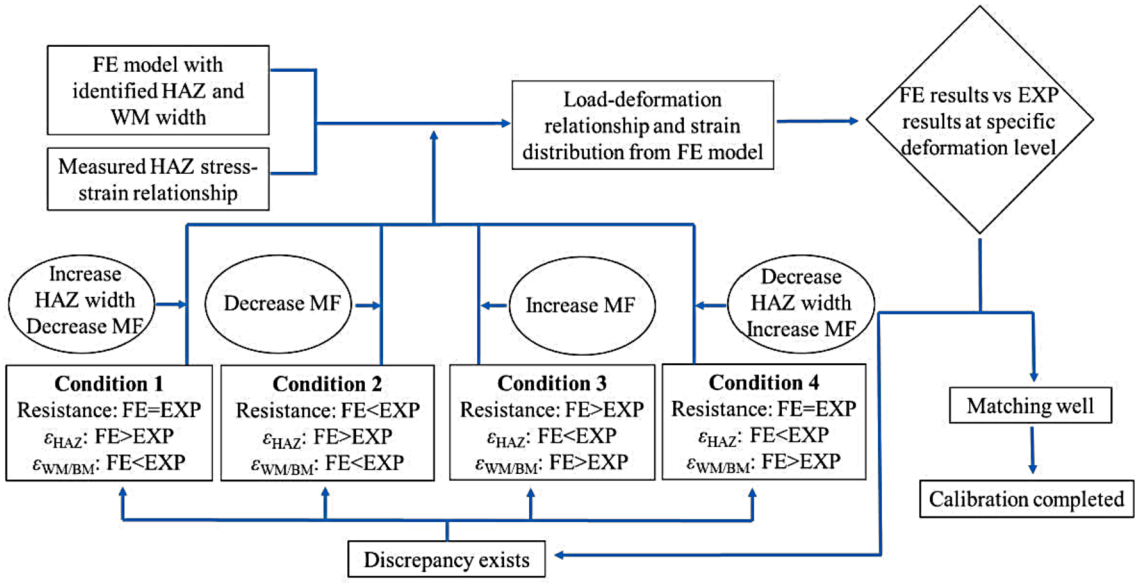

Fig. 9. The complete calibration procedures.

4.1. *Modification factor calibration*

The modification factor is calibrated by a trial-and-error process based on the load-deformation relationship and the strain distribution plot at two deformation levels. Fig. 8 presents three typical strain distribution plots during the calibration. The black solid line is the experimental result. The blue and the red dash line represents the FE result using the measured original HAZ material property and the modified material property, respectively.

First, the FE model is created based on the measured and identified dimensions (HAZ and WM width), as illustrated in Section 3. The measured original HAZ stress–strain relationship is used in FEA for the first trial. If the predicted resistance is higher than the experiment for a specific deformation level, a modification factor is needed, shown as Condition 3 in Fig. 9. Meanwhile, the predicted strain in HAZ is smaller while larger in BM and WM than the experiment shown as the blue dash line in Fig. 8. Therefore, in the second step, a modification factor should be applied to reduce the stress. Depending on the deviation level, the increment of the modification factor can be 3% in the beginning and gradually reduce to 1% in the subsequent iteration steps. The resistance and the strain distribution at the specific deformation level predicted by FEA should match the experimental results well if an appropriate modification factor is used. The strain distribution of FE results using the modified HAZ material property is presented by the red dash line in Fig. 8 a). The matching level is evaluated visually since the strain distribution shows an adequate difference with a 1% modification factor increment, which is the minimum increment used in this research. A cost function can be used to calibrate the modification factor with a finer increment. However, the current research object is to establish a HAZ stress–strain relationship suitable for FEA of large scale welded tubular joints. The evaluation approach is sufficient considering the efficiency and the accuracy. If an excessive modification factor is applied, such as Condition 2 in Fig. 9, the predicted strain in HAZ and the predicted resistance would be greater and smaller, respectively, than the experiment. By repeating the second step, an appropriate modification factor could be calibrated. Note that if BM and WM impose a limited transverse constraint on HAZ, the modification factor may not be necessary. Consequently, the FE strain distribution may fit the experimental result well using the measured original HAZ stress–strain relationship.

This calibration procedure should be done at least at the early hardening stage (0.5 mm deformation in this study) and the onset of the necking for calibrating the linear modification factor. More deformation levels should be involved in the calibration if a non-linear modification factor is required.

In addition, the identified HAZ width used in the FE model may slightly deviate from the experiment, given the accuracy of the DIC measurement. The width deviation could be eliminated in the calibration procedures. Fig. 8 b) and c) show the strain distribution in the FE model with a narrower and a wider HAZ, respectively. The red dash line represents the strain distribution of the FE model, where the modified

Table 6
The adjusted width of HAZ and WM [mm].

Code-name	S700t8	S700t10	S500t8	S500t10	S355t8	S355t10
HAZ_1	4	3.5	4	5	4	2.5
HAZ_2	3	2.5	4.5	4	3.5	3
WM	9.5	10	8.5	9	14.5	12

stress–strain relationship is used, and the predicted resistance fit the experiment at a specific deformation level. Take the FE model with a narrower HAZ width, for example. The narrower HAZ width in the FE model results in a higher level of the transverse constraint from BM and WM. Hence, a more significant modification factor is required for accurately predicting the resistance, leading to the excessive strain localisation in HAZ, corresponding to Condition 1 in Fig. 9. By slightly increasing the HAZ width with 0.5 mm increment, a smaller modification factor is required for fitting the resistance, and the problem of the excessive strain localisation in HAZ is solved. The adjusted width of HAZ and WM is summarised in Table 6. In the presented investigation, by 5 to 10 iterations, the HAZ constitutive model and width could be determined. A detailed flowchart illustrating the complete calibration procedures is shown in Fig. 9.

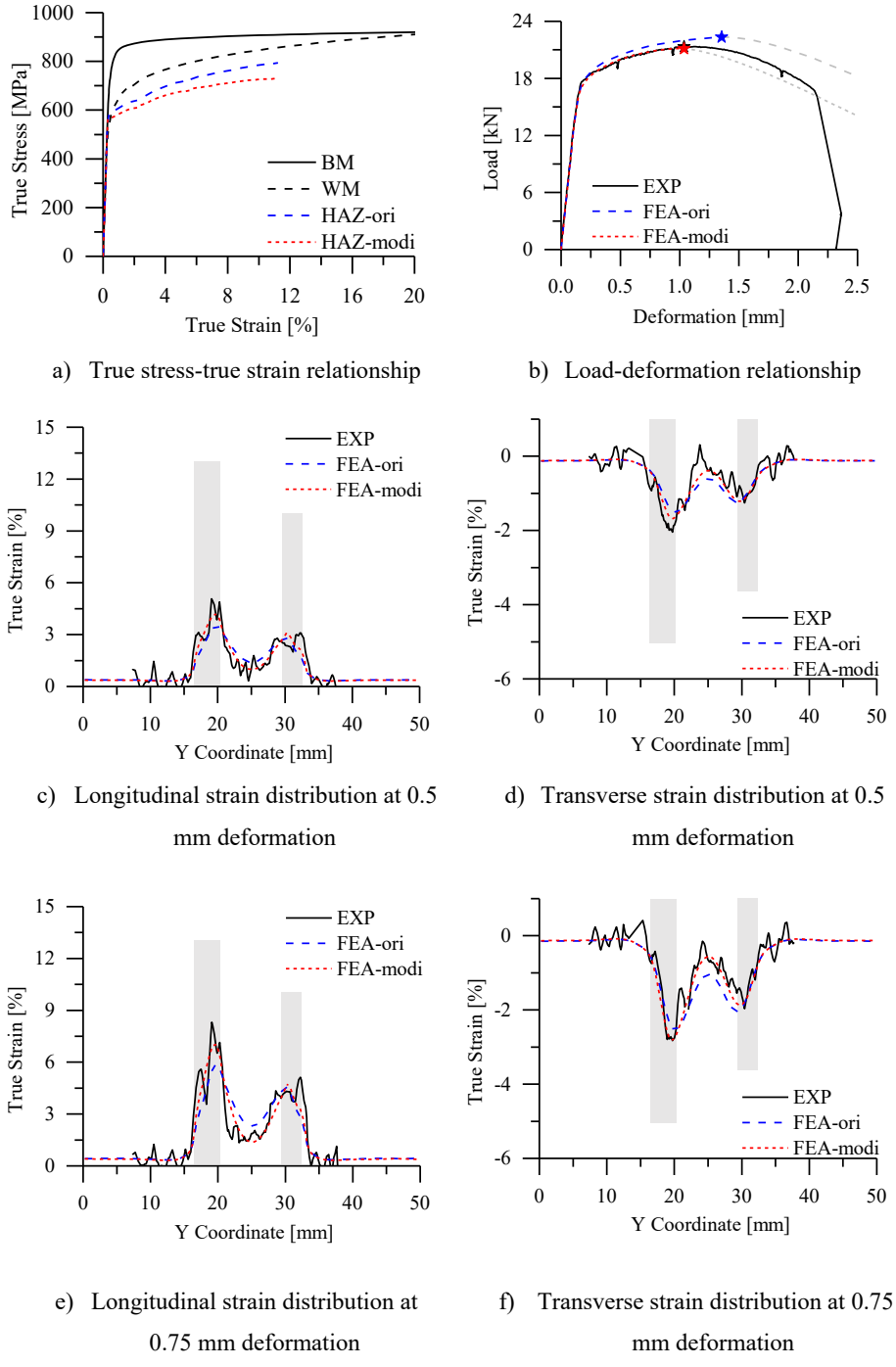

a) True stress-true strain relationship

b) Load-deformation relationship

c) Longitudinal strain distribution at 0.5 mm deformation

d) Transverse strain distribution at 0.5 mm deformation

e) Longitudinal strain distribution at 0.75 mm deformation

f) Transverse strain distribution at 0.75 mm deformation

Fig. 10. Comparison of FE and DIC results (S700t8).

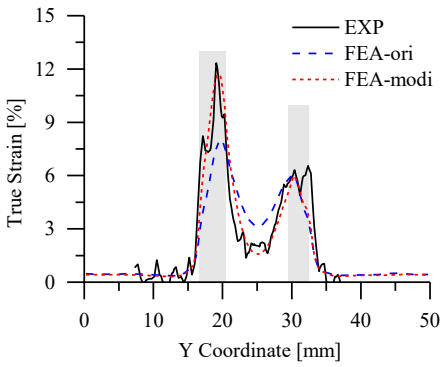

g) Longitudinal strain distribution at 1.04 mm deformation

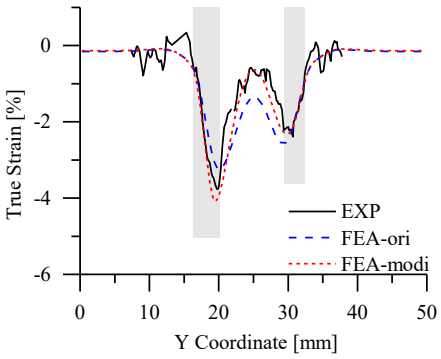

h) Transverse strain distribution at 1.04 mm deformation

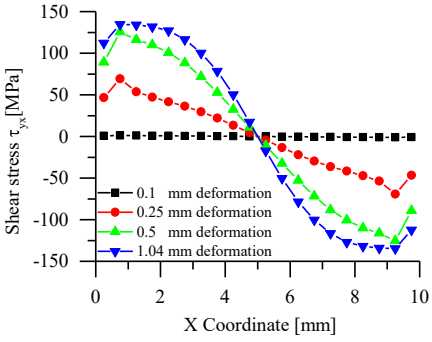

i) hear stress distribution in HAZ at HAZ -BM boundary (FEA-modi)

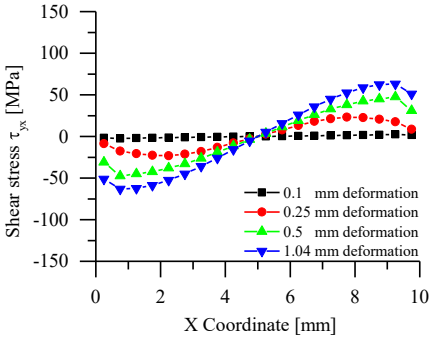

j) Shear stress distribution in HAZ at HAZ -WM boundary (FEA-modi)

Fig. 10. (*continued*).

4.2. Calibration results

The results of two FEAs, FEA-ori and FEA-modi, are compared to the experimental results in Figs. 10-12. FEA-ori uses the measured original HAZ material property without the modification factor, while FEA-modi uses the modified true stress-true strain relationship of HAZ with the calibrated modification factor.

The load-deformation curves obtained from the experiment and FEA are compared in Figs. 10-12 b). A solid "Star" symbol is used to show the ultimate resistance point, at which HAZ reaches the necking strain, for each curve. After the " Star " symbol, the post-necking part of the FE result is shown with a grey colour. Note that further damage model analysis is required for fitting the post-necking part of the curve.

Two longitudinal true strain distribution diagrams at two levels of the longitudinal deformation, which are used for calibrating the modification factor, are presented in Figs. 10-12 c) and g) for each specimen. The first deformation level is 0.5 mm and corresponds to the early hardening stage. The second deformation level corresponds to the ultimate resistance obtained in the experiment. The longitudinal strain distribution at the middle of the abovementioned two deformation levels is investigated for validation, as shown in Figs. 10-12 e). Besides, the corresponding transverse true strain distributions at the three deformation levels are presented in Figs. 10-12 d), f), and h), which are used to evaluate the validity of the Mises yield criterion considering the material anisotropy in the weld region. The region of two HAZs is marked with a grey background in these true strain distribution plots. It has to be clarified that the same stress–strain relationship is used in two HAZs of each specimen (with the same modification factors). The difference in the maximum strain of two HAZs results from the different widths of two HAZs.

The coordinate system in FE model is positioned such that the necking always appears in the left HAZ referring to Fig. 7 a). Therefore, the shear stress (τ_{yx}) in the left HAZ at two boundary surfaces is investigated to illustrate the level of the transverse constraint based on FEA-modi. The shear stress distribution in HAZ boundary elements close to BM and WM are presented in Figs. 10-12 i) and j), respectively. The elements are in the central layer of HAZ, as presented in Fig. 7 c). The shear stress is positive if it acts on a positive face in a positive direction or if it acts on a negative face in a negative direction. In addition to the two levels of the longitudinal deformation for obtaining the true strain distribution, two more levels at the elastic stage (0.1 mm) and the onset of the yielding (0.25 mm) are investigated.

The detailed result of the specimen with 8 mm original nominal thickness (before milling) for different steel grades is discussed below. The calibrated modification factor and the evaluation of the deviation between experiments and FEA predictions for all six specimens are presented in Table 10 at the end of this section.

4.2.1. S700t8 welded coupon specimen (undermatching weld)

Fig. 10 a) presents the true stress-true strain relationship of different regions used in the FEA of the S700t8 welded coupon specimen. The black solid and dash lines represent BM and WM, respectively. The blue dash line, namely HAZ-ori, is the original relationship without the stress modification, while the red dash line is the modified relationship with the reduced true stress. The modification factors MF_1 and MF_2 are 4% and 8%, respectively. From Fig. 10 a), it is evident that BM and WM are

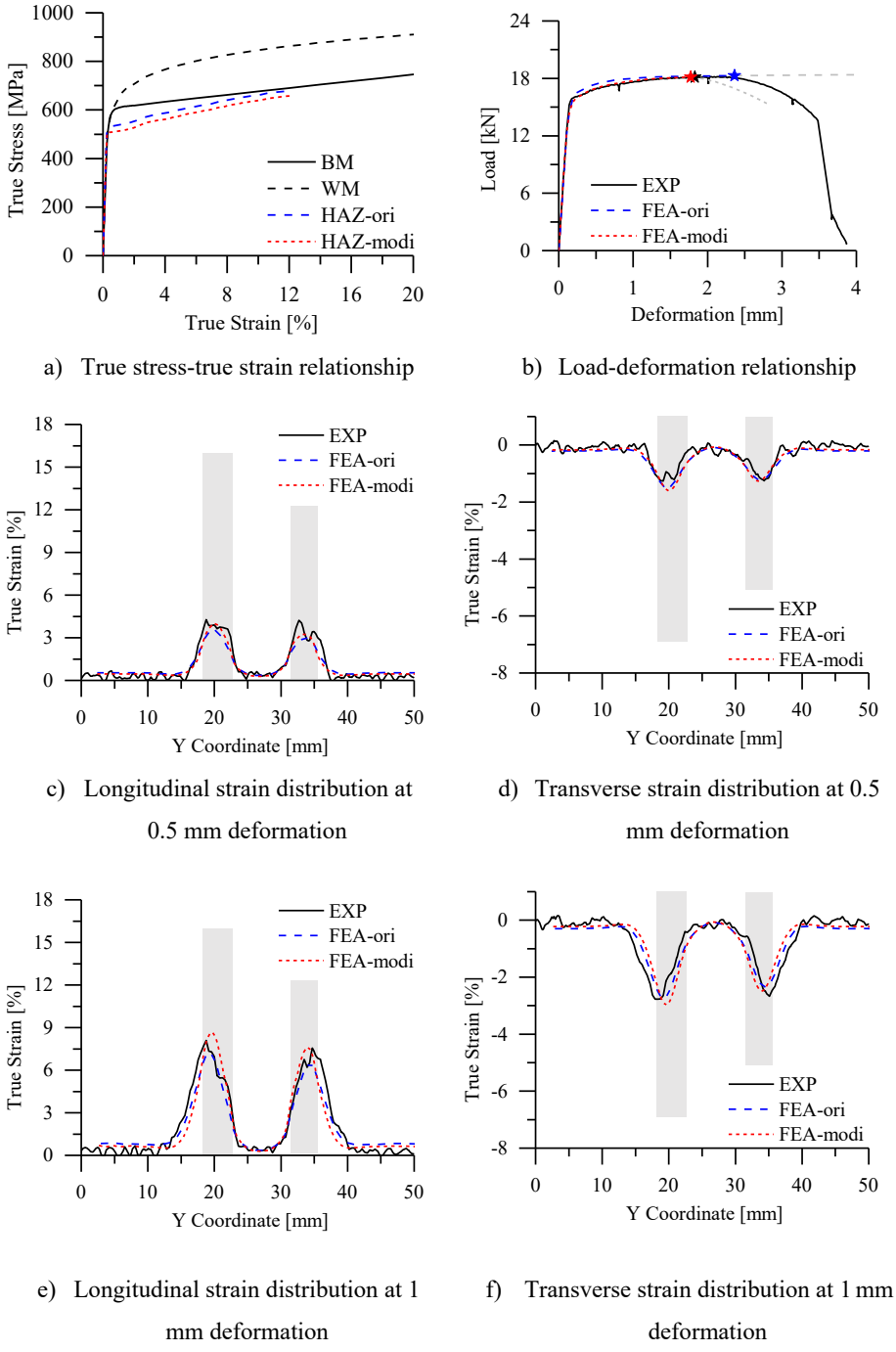

a) True stress-true strain relationship

b) Load-deformation relationship

c) Longitudinal strain distribution at 0.5 mm deformation

d) Transverse strain distribution at 0.5 mm deformation

e) Longitudinal strain distribution at 1 mm deformation

f) Transverse strain distribution at 1 mm deformation

Fig. 11. Comparison of FE and DIC results (S500t8).

stronger than HAZ. BM and WM would experience a limited plastic strain as HAZ reaches the necking point. The level of the transverse constraint increases during loading since the HAZ hardening performance (tangent of the true stress-true strain curve) reduces with the increase of the true strain. It can also be proved by Fig. 10 i) and j) where the shear stress imposed by BM and WM increases with the level of the deformation, indicating that the transverse constraint keeps increasing during loading. Consequently, the modification factor ascends with the increase of the true strain, conforming to the case in Fig. 6 a). It must be clarified that the transverse constraint does not exist at the elastic stage since the shear stress is nearly 0 MPa at 0.1 mm deformation. The non-existing transverse constraint at the elastic stage could also be observed in specimens S500t8 and S355t8.

The load-deformation relationship obtained from the experiment and FEA based on 50 mm gauge length is compared in Fig. 10 b). The ultimate resistance and the corresponding deformation (peak deformation) are shown in Table 7. FEA-ori has a 5% higher resistance and 30% higher peak deformation compared to the experimental results. Using the modified HAZ property, the ultimate resistance is 1% lower than the experimental results and the peak deformation is well predicted with 0% deviation.

The true strain in the longitudinal direction (ε_y) and the transverse direction (ε_x) is extracted from elements (in DIC and FE model) in the middle of the specimen surface, as shown in Fig. 7 b). The longitudinal

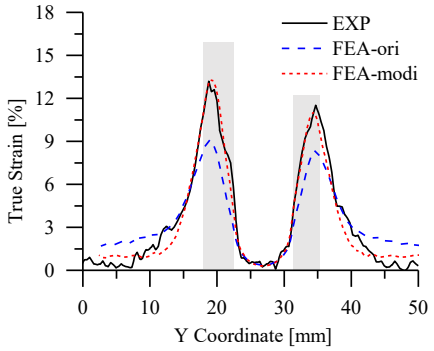

g) Longitudinal strain distribution at 1.7 mm deformation

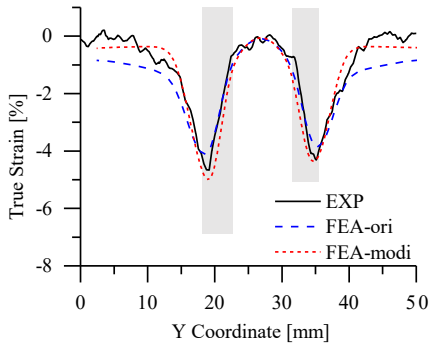

h) Transverse strain distribution at 1.7 mm deformation

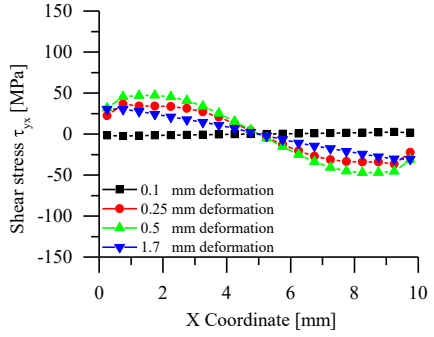

i) Shear stress distribution in HAZ at HAZ -BM boundary (FEA-modi)

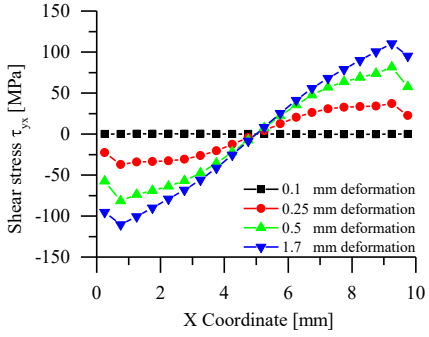

j) Shear stress distribution in HAZ at HAZ -WM boundary (FEA-modi)

Fig. 11. (*continued*).

true strain distribution at 0.5 mm, 0.75 mm, and 1.04 mm (corresponding to the ultimate resistance in the experiment) deformation is plotted against the elements' Y-coordinate in Fig. 10 c), e), and g), respectively. Compared to the experiments, results from FEA-ori have a smaller strain in HAZ while a larger strain in WM. It indicates that the HAZ strength is overestimated at all deformation stages, resulting in a higher resistance and consequently a higher strain level in WM and BM. With the same total deformation, the contribution from each region to the total deformation is different between FEA-ori and the experiment. Using the modified material property, the true strain distribution of FEA-modi matches the experimental result much better. Besides, the transverse strain in experiments and FEA are compared in Fig. 10 d), f), and h). Good agreements are observed, demonstrating that HAZ and WM can be modelled as isotropic materials that follow the Mises yield criterion. Therefore, the modified HAZ stress–strain relationship is successfully calibrated until the onset of necking. In addition, considering all 6 true strain plots, it can be seen that the peak strain in HAZ does not appear in the middle of each HAZ but is slightly close to the side (BM or WM) with a weaker material which is WM in this case. This strain pattern also exists in S500 and S355 specimens.

4.2.2. S500t8 welded coupon specimen (overmatching weld)

The true stress–strain relationship of different materials is shown in Fig. 11 a). MF_1 and MF_2 are 5% and 3%, respectively. Since the strain hardening of BM is relatively low, the true stress of BM and HAZ gets closer when the true strain approaches the HAZ necking strain, as shown in Fig. 11 a). In Fig. 11 i), the shear stress on the BM-HAZ side decreases as the deformation approaches the ultimate stage. Therefore, the level of the transverse constraint reduces, and the modification factor descends with the increase of the true strain, aligning with the case in Fig. 6 b). Besides, Fig. 11 i) and j) illustrate that the constraint level on the WM side is larger than the BM side, indicating that an overmatching weld was applied.

Fig. 11 b) presents the load-deformation relationship obtained from FEA and the experiment. The model (FEA-ori) with the original HAZ property has a higher resistance at the beginning of the plastic stage, while the ultimate resistance is very close to the experimental result (1% deviation). However, the peak deformation of FEA-ori is 28% larger than the experimental results, as shown in Table 8. In Fig. 11 g), the strain in BM of FEA-ori is much higher than that of the experiment, resulting in a hugely overestimated deformation in BM. Using the modified constitutive model, FEA-modi underestimates the peak deformation by 3% while the ultimate resistance is well predicted with 0% deviation, as presented in Table 8. In addition, the overestimated resistance at the beginning of the plastic stage is corrected by using the modified constitutive model.

Similar to the S700t8 welded coupon specimen, the strain in HAZ predicted by FEA-ori is smaller than that of the experiment at three deformation stages (0.5 mm, 1 mm, and 1.7 mm), as shown in Fig. 11 c), e), and g). Using the modified material property, the strain distribution predicted by FEA-modi matches the experimental result well. Fig. 11 c), e), and g) also demonstrate that HAZ and WM are the isotropic material following the Mises yield criterion. Therefore, it can be concluded that the stress reduced property of HAZ is successfully calibrated until the onset of necking.

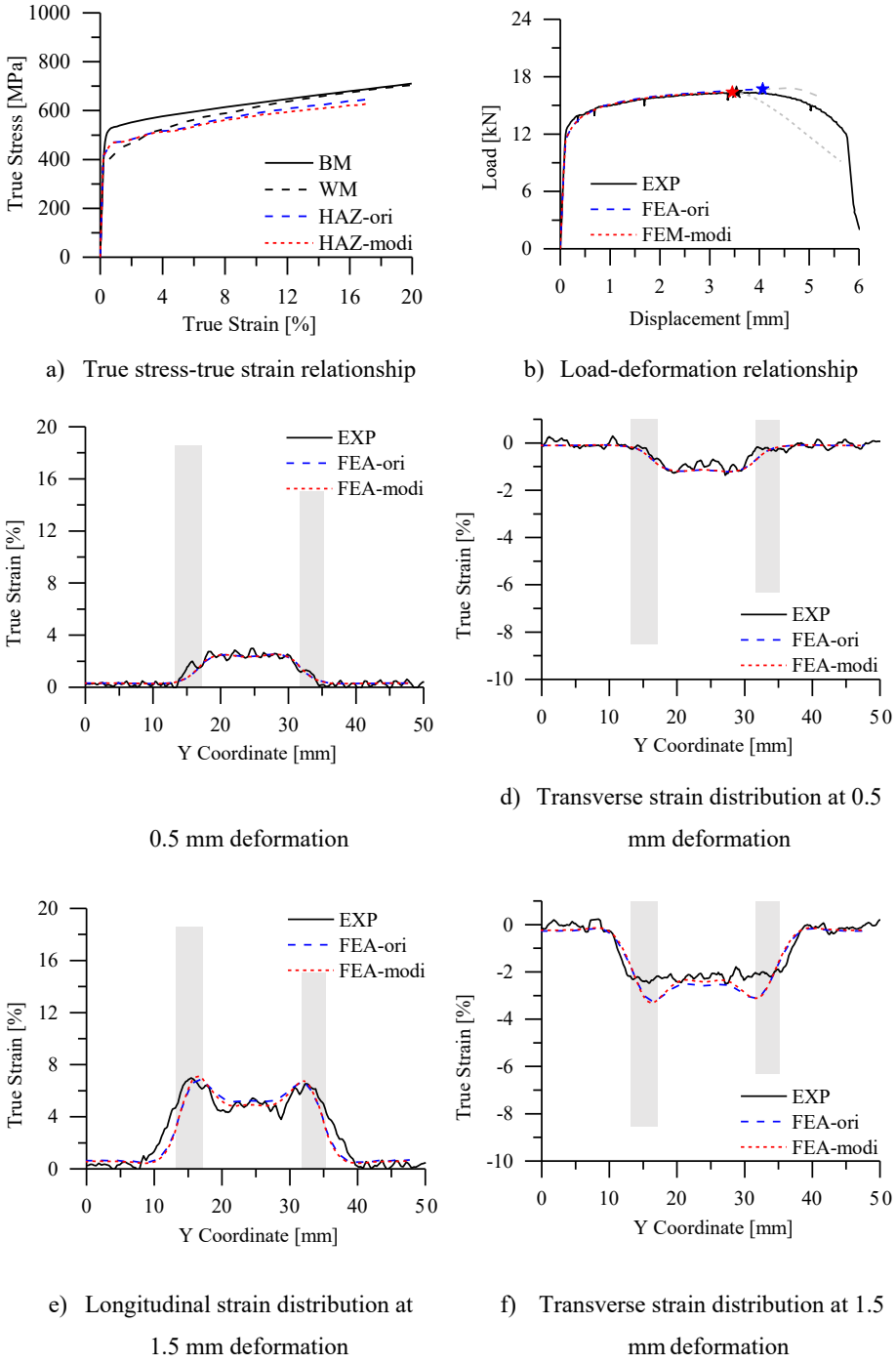

a) True stress-true strain relationship

b) Load-deformation relationship

0.5 mm deformation

d) Transverse strain distribution at 0.5 mm deformation

e) Longitudinal strain distribution at 1.5 mm deformation

f) Transverse strain distribution at 1.5 mm deformation

Fig. 12. Comparison of FE and DIC results (S355t8).

4.2.3. S355t8 welded coupon specimen (matching weld)

WM yields at a lower strength compared to HAZ, as shown in Fig. 12 a). Therefore, MF_1 is 0%. The 0% modification factor can also be justified by Fig. 12 c), where the strain distribution obtained from FEA-ori matches the experimental result well. Fig. 12 a) shows that WM has a stronger hardening performance than HAZ. Thus, the transverse constraint increases during the loading. At the onset of necking, the underestimated strain, consequently the overestimated stress, could be observed in Fig. 12 g) where the strain in FEA-ori HAZ is smaller than the experiment. Based on the parametric study, a 4% reduction is calibrated for MF_2. Fig. 12 i) and j) demonstrate that the shear stress is relatively low at the beginning of plastification, and it increases to its maximum at the onset of the necking. A similar shear stress level is observed on BM and WM sides, indicating that the joint has a matching weld. Therefore, the modification factor is in an ascending trend matching the situation in Fig. 6 a). Besides, since WM has a lower yield strength than HAZ, HAZ imposes a transverse constraint on WM presented by curves with 0.25 mm and 0.5 mm deformation in Fig. 12 j).

The load-deformation relationships obtained from FEA and experiments are compared in Fig. 12 b). The ultimate resistance and the peak deformation are presented in Table 9. The ultimate resistance predicted by FEA-ori shows a good agreement with the experimental result within

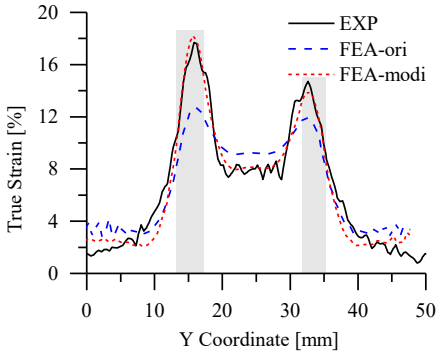

g) Longitudinal strain distribution at 3.5 mm deformation

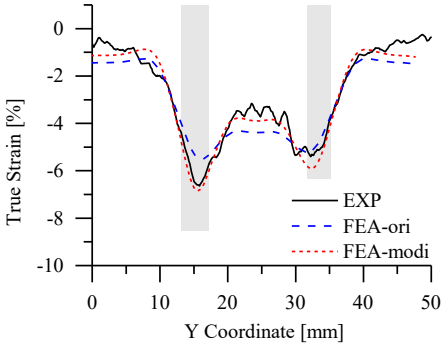

h) Transverse strain distribution at 3.5 mm deformation

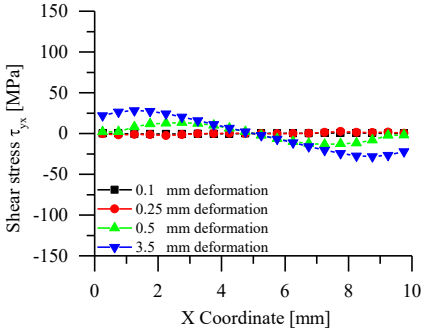

i) Shear stress distribution in HAZ at HAZ -BM boundary (FEA-modi)

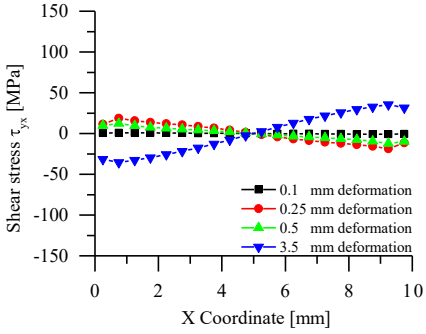

j) Shear stress distribution in HAZ at HAZ -WM boundary (FEA-modi)

Fig. 12. (*continued*).

Table 7
Comparison of the ultimate resistance and the peak deformation (S700t8).

	EXP	FEA-ori	FEA - ori / EXP	FEA-modi	FEA - modi / EXP
Ultimate resistance	21.31 kN	22.33 kN	1.05	21.11 kN	0.99
Peak deformation	1.04 mm	1.35 mm	1.30	1.04 mm	1.00

Table 8
Comparison of the ultimate resistance and the peak deformation (S500t8).

	EXP	FEA-ori	FEA - ori / EXP	FEA-modi	FEA - modi / EXP
Ultimate resistance	18.13 kN	18.28 kN	1.01	18.11 kN	1.00
Peak deformation	1.83 mm	2.35 mm	1.28	1.77 mm	0.97

a 3% deviation. However, the peak deformation of FEA-ori is 14% larger than that of the experiment. With a modified material property, FEA-modi predicts the peak deformation 3% smaller than that of the experiment, while the ultimate resistance is predicted with a 0% deviation.

In Fig. 12 c), e), and g), the longitudinal strain distributions at three deformation stages (0.5 mm deformation at the beginning of the plastic stage, 1.5 mm at the middle of the hardening stage, and 3.5 mm at the ultimate load) predicted by FEA-modi with the stress reduced material property show good agreement with the experimental results. Besides, the HAZ and WM material isotropy are demonstrated in Fig. 12 d), f), and h). Therefore, it is concluded that the modified material property of HAZ is successfully calibrated until the onset of necking.

Table 9
Comparison of the ultimate resistance and the peak deformation (S355t8).

	EXP	FEA-ori	FEA - ori / EXP	FEA-modi	FEA - modi / EXP
Ultimate resistance	16.35 kN	16.83 kN	1.03	16.38 kN	1.00
Peak deformation	3.54 mm	4.05 mm	1.14	3.45 mm	0.97

4.3. Discussion on results

This section compares the results of two FEAs using the HAZ property with and without the calibrated linear modification factor to the experimental result measured by DIC. The calibrated modification factor, the deformation ratio, and the resistance ratio are summarised in Table 10. The ultimate resistance predicted by FEA using the original HAZ material property is slightly higher than the experimental result within a maximum 5% deviation. However, the peak deformation is overestimated by at least 14% among all specimens, except for the specimen S500t10 where the BM material property is relatively soft resulting in a 0% MF_2.

In the scope of this experimental and numerical investigation, FEA-ori of the S700 specimen with an undermatching weld has the most

Table 10
Summary of the calibrated parameters and the prediction results.

Specimen	$\frac{R_{ori}}{R_{EXP}}$	$\frac{D_{ori}}{D_{EXP}}$	$\frac{R_{modi}}{R_{EXP}}$	$\frac{D_{modi}}{D_{EXP}}$	MF_1 [%]	MF_2 [%]	ε_1 [%]	ε_2 [%]
S700t8	1.05	1.30	0.99	1.00	4	8	0.51	11.25
S700t10	1.04	1.29	0.99	1.00	4	6	0.52	9.16
S500t8	1.01	1.28	1.00	0.97	5	3	0.45	12.17
S500t10	1.00	1.03	1.00	0.98	5	0	0.49	10.04
S355t8	1.03	1.14	1.00	0.97	0	4	0.41	17.05
S355t10	1.02	1.19	1.00	0.97	0	5	0.44	14.97

where R_i/R_{EXP} and D_i/D_{EXP} (i = ori or modi) are the resistance ratio and the deformation ratio, respectively.

significant overestimation (averagely 30%) on the peak deformation. Consequently, a large modification factor, with a combination of an average 4% MF_1 and 7% MF_2, is applied to the HAZ material property. For the S500 material with an overmatching weld, a descending linear modification factor with a 5% MF_1 and 2% MF_2 combination is obtained. For the S355 material with a matching weld, MF_1 is 0% since WM has a lower yield strength than HAZ. The modification factor increases to an average of 5% at the onset of necking. The deformation is overestimated at around 17% by FEA-ori.

Using the calibrated modification factor, the ultimate resistance and the peak deformation predicted by FEA-modi has a maximum 1 % and 3% deviation from the experiment, respectively. Although the FE model with the calibrated modification factor is validated against the experiment, it is essential to calibrate the modification factor for other welded joints with different steel grades and filler metals to accurately predict the deformation in the weld zone, consequently the deformation capacity of the welded joint.

5. Conclusions and future work

The constitutive model of the heat-affected zone (HAZ) was evaluated experimentally and numerically in this study. A linear true stress modification factor, as a function of the true strain, is proposed to eliminate the effect of the transverse constraint. Based on the presented results, the following conclusions are drawn:

1. The weld metal (WM) and/or the base material (BM) impose a transverse constraint on HAZ regardless of the steel grade if HAZ is the weakest component of a welded joint. The larger difference in the material hardening behaviour between HAZ and WM and/or BM, the heavier the transverse constraint is. It leads to a higher overestimation of the HAZ material strength monitored by the digital image correlation (DIC).
2. Using the measured HAZ stress–strain relationship, the finite element (FE) model using the original measured HAZ material property (FEA-ori) predicts a reasonably correct ultimate resistance within 5% overestimate, while the peak deformation, corresponding to the onset of HAZ necking, could be overestimated up to 30%. The overestimation of the peak deformation would be even more significant with a longer measuring range.
3. A linear modification factor is proposed to modify (reduce) the true stress of the measured HAZ material property. A combination of an average 4% MF_1 (at yielding) and 7% MF_2 (at the onset of necking) modification factor is calibrated for S700 material. MF_1 and MF_2 are on average 5% and 2% for S500 material, respectively. For S355 material, the modification factors MF_1 and MF_2 are 0% and 5% on average, respectively.
4. HAZ and WM are “sufficiently” the isotropic material, and therefore the Mises yield criterion is suitable.
5. Although the modification factor is validated for three steel grades in this study, it is essential to calibrate the modification factor for other welded joints made of different steel grades, filler metals, and welding procedures. The true strain distribution along the loading direction and the load-deformation relationship obtained from DIC and FEA should be used to validate the material property before necking. Damage modelling is required to model the joint behaviour properly after necking.

In future work, the proposed method will be used to generate the true constitutive model of HAZ from more tensile tests of welded specimens. The corrected material property is used in advanced FEA of various welded tubular joints [42], where the damage modelling is applied to analyse the failure of welded joints. Besides, the same calibration procedure could be used to evaluate different constraint levels of different steel grades, matching types and HAZ widths. Consequently, the HAZ strength reduction factor k_{HAZ} in prEN1993-1–12 [34] could be appropriately determined for high strength and ultra-high strength steel welded joints.

CRediT authorship contribution statement

Rui Yan: Conceptualization, Data curation, Formal analysis, Methodology, Investigation, Software, Validation, Visualization, Writing – original draft, Writing – review & editing. **Haohui Xin:** Writing – review & editing. **Fei Yang:** Writing – review & editing. **Hagar El Bamby:** Data curation, Writing – review & editing. **Milan Veljkovic:** Conceptualization, Supervision, Writing – review & editing. **Kristo Mela:** Writing – review & editing.

Declaration of Competing Interest

The authors declare that they have no known competing financial interests or personal relationships that could have appeared to influence the work reported in this paper.

Acknowledgements

The authors would like to thank the company SSAB Europe for the financial support during this investigation.

References

[1] R. Yan, H. El Bamby, M. Veljkovic, H. Xin, F. Yang, A method for identifying the boundary of regions in welded coupon specimens using digital image correlation, Materials & Design. 210 (2021), 110073, https://doi.org/10.1016/j.matdes.2021.110073.
[2] A. Khalfallah, Experimental and numerical assessment of mechanical properties of welded tubes for hydroforming, Materials and Design. 56 (2014) 782–790, https://doi.org/10.1016/j.matdes.2013.11.051.
[3] M.L. Zhu, F.Z. Xuan, Correlation between microstructure, hardness and strength in HAZ of dissimilar welds of rotor steels, Materials Science and Engineering A. 527 (2010) 4035–4042, https://doi.org/10.1016/j.msea.2010.03.066.
[4] Y. Peng, C. Wu, J. Gan, J. Dong, Characterization of heterogeneous constitutive relationship of the welded joint based on the stress-hardness relationship using micro-hardness tests, Construction and Building Materials. 202 (2019) 37–45, https://doi.org/10.1016/j.conbuildmat.2018.12.218.
[5] D. Tabor, The hardness of metals, Oxford University Press, 1951.
[6] M. Amraei, S. Afkhami, V. Javaheri, J. Larkiola, T. Skriko, T. Björk, X.-L. Zhao, Mechanical properties and microstructural evaluation of the heat-affected zone in ultra-high strength steels, Thin-Walled Structures. 157 (2020) 107072.
[7] R.M. Molak, K. Paradowski, T. Brynk, L. Ciupinski, Z. Pakiela, K.J. Kurzydlowski, Measurement of mechanical properties in a 316L stainless steel welded joint,

International Journal of Pressure Vessels and Piping. 86 (2009) 43–47, https://doi.org/10.1016/j.ijpvp.2008.11.002.
[8] J. Kim, Y.-W. Kim, B.-S. Kang, S.-M. Hwang, Finite element analysis for bursting failure prediction in bulge forming of a seamed tube, Finite Elements in Analysis and Design. 40 (2004) 953–966, https://doi.org/10.1016/j.
[9] M. Flansbjer, T. Sjögren, Using digital image correlation techniques and finite element models for strain-field analysis of a welded aluminium structure, Applied Mechanics and Materials. 70 (2011) 123–128, https://doi.org/10.4028/www.scientific.net/AMM.70.123.
[10] C. Chen, S.P. Chiew, M.S. Zhao, C.K. Lee, T.C. Fung, Welding effect on tensile strength of grade S690Q steel butt joint, Journal of Constructional Steel Research. 153 (2019) 153–168, https://doi.org/10.1016/j.jcsr.2018.10.009.
[11] C. Chen, S.P. Chiew, M.S. Zhao, C.K. Lee, T.C. Fung, Influence of cooling rate on tensile behaviour of S690Q high strength steel butt joint, Journal of Constructional Steel Research. 173 (2020), 106258, https://doi.org/10.1016/j.jcsr.2020.106258.
[12] M. Amraei, T. Skriko, T. Björk, X.L. Zhao, Plastic strain characteristics of butt-welded ultra-high strength steel (UHSS), Thin-Walled Structures. 109 (2016) 227–241, https://doi.org/10.1016/j.tws.2016.09.024.
[13] F. Farrokhi, J. Siltanen, A. Salminen, Fiber Laser Welding of Direct-Quenched Ultrahigh Strength Steels: Evaluation of Hardness, Tensile Strength, and Toughness Properties at Subzero Temperatures, Journal of Manufacturing Science and Engineering, Transactions of the ASME 137 (2015) 1–10, https://doi.org/10.1115/1.4030177.
[14] R. Stroetmann, T. Kästner, A. Hälsig, P. Mayr, Influence of the cooling time on the mechanical properties of welded HSS-joints, Steel, Construction. 11 (2018) 264–271, https://doi.org/10.1002/stco.201800019.
[15] F. Hochhauser, W. Ernst, R. Rauch, R. Vallant, N. Enzinger, Influence of the soft zone on the strength of welded modern HSLA steels, Welding in the World. 56 (5-6) (2012) 77–85.
[16] A.P. Reynolds, F. Duvall, Digital image correlation for determination of weld and base metal constitutive behavior, Welding Journal (Miami, Fla) 78 (1999) 355-s.
[17] W.D. Lockwood, B. Tomaz, A.P. Reynolds, Mechanical response of friction stir welded AA2024: Experiment and modeling, Materials Science and Engineering A. 323 (2002) 348–353, https://doi.org/10.1016/S0921-5093(01)01385-5.
[18] W.D. Lockwood, A.P. Reynolds, Simulation of the global response of a friction stir weld using local constitutive behavior, Materials Science and Engineering A. 339 (2003) 35–42, https://doi.org/10.1016/S0921-5093(02)00116-8.
[19] M.A. Sutton, J.H. Yan, S. Avril, F. Pierron, S.M. Adeeb, Identification of heterogeneous constitutive parameters in a welded specimen: Uniform stress and virtual fields methods for material property estimation, Experimental Mechanics. 48 (2008) 451–464, https://doi.org/10.1007/s11340-008-9132-6.
[20] R. Bai, Y. Wei, Z. Lei, H. Jiang, W. Tao, C. Yan, X. Li, Local zone-wise elastic-plastic constitutive parameters of Laser-welded aluminium alloy 6061 using digital image correlation, Optics and Lasers in Engineering. 101 (2018) 28–34, https://doi.org/10.1016/j.optlaseng.2017.09.023.
[21] X. Wu, J. Shuai, K. Xu, Z. Lv, Local Constitutive Behavior of Undermatched Welded Joints in Pipeline Steel Using Digital Image Correlation Technology, Journal of Pressure Vessel Technology, Transactions of the ASME. 142 (2020) 1–6, https://doi.org/10.1115/1.4047271.
[22] Y. Peng, C. Wu, J. Gan, J. Dong, Determination of the local constitutive properties of the welded steel joints using digital image correlation method, Construction and Building Materials. 171 (2018) 485–492, https://doi.org/10.1016/j.conbuildmat.2018.03.182.
[23] G. Li, F. Xu, G. Sun, Q. Li, Identification of mechanical properties of the weld line by combining 3D digital image correlation with inverse modeling procedure, International Journal of Advanced Manufacturing Technology. 74 (2014) 893–905, https://doi.org/10.1007/s00170-014-6034-x.
[24] M.I. Costa, D.M. Rodrigues, C. Leitão, Analysis of AA 6082–T6 welds strength mismatch: stress versus hardness relationships, International Journal of Advanced Manufacturing Technology. 79 (2015) 719–727, https://doi.org/10.1007/s00170-015-6866-z.
[25] C. Leitão, I. Galvão, R.M. Leal, D.M. Rodrigues, Determination of local constitutive properties of aluminium friction stir welds using digital image correlation, Materials and Design. 33 (2012) 69–74, https://doi.org/10.1016/j.matdes.2011.07.009.
[26] G.L. Louëdec, F. Pierron, M.A. Sutton, A.P. Reynolds, Reynolds, Identification of the Local Elasto-Plastic Behavior of FSW Welds Using the Virtual Fields Method 53 (5) (2013) 849–859.
[27] N. Milošević, A. Sedmak, I. Martić, R. Prokić-Cvetković, Novel procedure to determine actual stress-strain curves, Structural Integrity and Life. 21 (2021) 37–40.
[28] N.Z. Milošević, A.S. Sedmak, G.M. Bakić, V. Lazić, M. Milošević, G. Mladenović, A. Maslarević, Determination of the actual stress–strain diagram for undermatching welded joint using dic and fem, Materials. 14 (16) (2021) 4691.
[29] G. Seon, A. Makeev, J.D. Schaefer, B. Justusson, Measurement of interlaminar tensile strength and elastic properties of composites using open-hole compression testing and digital image correlation, Applied Sciences (Switzerland). 9 (13) (2019) 2647.
[30] K. Denys, S. Coppieters, M. Seefeldt, D. Debruyne, Multi-DIC setup for the identification of a 3D anisotropic yield surface of thick high strength steel using a double perforated specimen, Mechanics of Materials. 100 (2016) 96–108, https://doi.org/10.1016/j.mechmat.2016.06.011.
[31] A. Lattanzi, A. Piccininni, P. Guglielmi, M. Rossi, A fast methodology for the accurate characterization and simulation of laser heat treated blanks, International Journal of Mechanical Sciences. 192 (2021) 106134. https://doi.org/10.1016/j.ijmecsci.2020.106134.
[32] B. Younise, A. Sedmak, M. Rakin, N. Gubeljak, B. Medjo, M. Burzić, M. Zrilić, Micromechanical analysis of mechanical heterogeneity effect on the ductile tearing of weldments, Materials and Design. 37 (2012) 193–201, https://doi.org/10.1016/j.matdes.2012.01.001.
[33] N. Milosevic, B. Younise, A. Sedmak, M. Travica, A. Mitrovic, Evaluation of true stress–strain diagrams for welded joints by application of Digital Image Correlation, Engineering Failure Analysis. 128 (2021), 105609, https://doi.org/10.1016/j.engfailanal.2021.105609.
[34] prEN 1993-1-12:2021 - Design of steel structures - Part 1-12: Additional rules for steel grades up to S960, 2021.
[35] Metallic materials - Tensile testing - Part 1: Method of test at room temperature (ISO 6892-1:2019), 1 (2019).
[36] S. Coppieters, T. Kuwabara, Identification of Post-Necking Hardening Phenomena in Ductile Sheet Metal, Experimental Mechanics. 54 (2014) 1355–1371, https://doi.org/10.1007/s11340-014-9900-4.
[37] J.H. Kim, A. Serpantié, F. Barlat, F. Pierron, M.G. Lee, Characterization of the post-necking strain hardening behavior using the virtual fields method, International Journal of Solids and Structures. 50 (2013) 3829–3842, https://doi.org/10.1016/j.ijsolstr.2013.07.018.
[38] H.W. Swift, Plastic instability under plane stress, Journal of the Mechanics and Physics of Solids. 1 (1952) 1–18, https://doi.org/10.1016/0022-5096(52)90002-1.
[39] Y. Ling, Uniaxial True Stress-Strain after Necking, AMP Journal of Technology. 5 (2004) 37–48.
[40] R. Yan, H. Xin, M. Veljkovic, Ductile fracture simulation of cold-formed high strength steel using GTN damage model, Journal of Constructional Steel Research. 184 (2021), 106832, https://doi.org/10.1016/j.jcsr.2021.106832.
[41] ABAQUS, Abaqus Analysis User's Manual, 2019 version, (2019).
[42] R. Yan, H. El Bamby, M. Veljkovic, K. Mela, Experimental and numerical investigation on tensile behaviour of welded tubular X-joints (in preparation), (n. d.).